Machine learning based prediction of melt pool morphology in a laser-based powder bed fusion additive manufacturing process

Article *in* International Journal of Production Research · April 2023

DOI: 10.1080/00207543.2023.2201860

5 authors, including:

Zhibo Zhang
University at Buffalo, The State University of New York

Chandan Kumar Sahu
University at Buffalo, The State University of New York

Rahul Rai
Clemson University

Zhuo Yang
National Institute of Standards and Technology

International Journal of Production Research

ISSN: (Print) (Online) Journal homepage: https://www.tandfonline.com/loi/tprs20

Machine learning based prediction of melt pool morphology in a laser-based powder bed fusion additive manufacturing process

Zhibo Zhang, Chandan Kumar Sahu, Shubhendu Kumar Singh, Rahul Rai, Zhuo Yang & Yan Lu

INTERNATIONAL JOURNAL OF PRODUCTION RESEARCH
https://doi.org/10.1080/00207543.2023.2201860

Machine learning based prediction of melt pool morphology in a laser-based powder bed fusion additive manufacturing process

Zhibo Zhang [a], Chandan Kumar Sahu [b], Shubhendu Kumar Singh[b], Rahul Rai [b], Zhuo Yang[c] and Yan Lu[d]

[a]Manufacturing and Design Lab (MADLab), University at Buffalo, Buffalo, NY, USA; [b]Geometric Reasoning and Artificial Intelligence Lab (GRAIL), Clemson University International Center for Automotive Research (CU-ICAR), Clemson, SC, USA; [c]Mechanical and Industrial Engineering Department, University of Massachusetts Amherst, Amherst, MA, USA; [d]National Institute of Standards and Technology, Gaithersburg, MD, USA

ABSTRACT

Laser-based powder bed fusion (L-PBF) has become the de facto choice for metal additive manufacturing (AM) processes. Even after considerable research investments, components manufactured using L-PBF lack consistency in their quality. Realizing the crucial role of the melt pool in controlling the final build quality, we predict the morphology of the melt pool directly from the build commands in an L-PBF process. We leverage machine learning techniques to predict quantitative attributes like the size as well as qualitative attributes like the shape of the melt pool. The area of the melt pool is predicted using an LSTM network. The outlined LSTM-based approach estimates the area with 90.7% accuracy. The shape is inferred by synthesising the images of the melt pool by using a Melt Pool Generative Adversarial Network (MP-GAN). The synthetic images attain a structural similarity score of 0.91. The precision and accuracy of the results showcase the efficacy of the outlined approach and pave the way for real-time monitoring and control of the melt pool to build products with consistently better quality.

ARTICLE HISTORY
Received 6 June 2022
Accepted 20 January 2023

KEYWORDS
Additive manufacturing; machine learning; in-situ monitoring; L-PBF; LSTM; GAN

1. Introduction

Additive manufacturing (AM) has evolved as a novel manufacturing paradigm because of its capability to offer additional design flexibility (Gupta and Rai 2014; Zhang et al. 2018) while reducing the supply chain (Kunovjanek and Reiner 2020), material wastage, assembly operations (Ghiasian et al. 2018) and tooling requirements. Laser-based powder bed fusion (L-PBF), a class of AM technology that uses a laser beam as the source of energy to selectively melt metallic powder in an inert chamber, is at the forefront of AM of metallic components (Khorram Niaki and Nonino 2017). In L-PBF, a thin layer of metallic powder is distributed over the build plate or any previous layer. Then, the laser traverses a predefined path while transmitting high-density energy to the powder at the target spot, thereby melting it. The molten metal locally coalesces and solidifies in horizontal (track-wise) and vertical (layer-wise) directions to form complex three-dimensional metallic components.

Several industries, including healthcare, aerospace, consumer products, and automotive, are trying to harness the promising potential of L-PBF AM processes. However, even after decades of research, the lack of guarantee of consistent quality and repeatability hinders the broader adoption of L-PBF. Additively manufactured parts are known to be porous and accumulate residual stresses (Khadilkar, Wang, and Rai 2019). Consequently, they exhibit subpar or a significant variation in the final mechanical properties. Undesired defects compromise the structural integrity and durability of the components, predominantly in biomedical and aerospace applications (Mower and Long 2016; Spierings, Starr, and Wegener 2013). While attributes like dimensional tolerances and surface roughness can be mitigated by appropriate postprocessing techniques (Jaiswal and Rai 2019), other attributes like porosity, spatter, balling, and residual stresses can only be minimised by monitoring and controlling the process in real-time as they manifest during the melting and solidification processes. Thus, AM calls for stringent in-situ quality control in real-time (Mani et al. 2017). Moreover, in-situ process monitoring will enable certification of the components as they are built. Consequently, in-situ process monitoring can reduce post-process destructive and nondestructive testing (Zhang et al. 2019) and material wastage (Ghiasian et al. 2018) due to scrapping.

CONTACT Rahul Rai rrai@clemson.edu Geometric Reasoning and Artificial Intelligence Lab (GRAIL), Clemson University International Center for Automotive Research (CU-ICAR), Clemson, SC 29634-0002, USA

The high-density energy supplied by the laser to the metal powder in an L-PBF process creates a pool of molten metal that coalesces and solidifies to form the final product. The melt pool initiates nucleation and microstructure formation and hence dictates the properties and performance of the built product. Thus, monitoring the melt pool is crucial as it is a signature of several underlying phenomena like the interaction of laser with metal powder, flow and dynamics of the melt pool, pool-powder interaction, and solidification. Most approaches for online in-situ monitoring of melt pools rely on thermographic or morphological information. Our work focuses on the latter due to non-invasive imaging techniques. The mechanical properties like strength and residual stresses depend on the thermal history during solidification, which in turn depends on the microstructural characteristics like melt pool morphology. Morphological features like the size, length, width, depth, and shape of the melt pool are essential features from which crucial information about the underlying phenomena can be inferred. The anomalies in the process (Yang and Rai 2019), and the onset of defects can be identified. Melt pools of smaller size (under-melt) increase the time of manufacturing. Smaller melt pools hinder fusion, thereby triggering porosity and balling phenomena. Melt pools with smaller widths can inhibit overlapping between adjacent tracks. Whereas shallower melt pools hinder inter-layer fusion, thereby contributing to porosity. Porosity is deterrent to tensile and fatigue strength (Kruth et al. 2007). Although larger melt pools (over-melt) can reduce the manufacturing time, they tend to increase porosity by vaporising the substrate (Kamath et al. 2014; Dilip et al. 2017). Hence, the area (size) of the melt pool is the most sought-after morphological feature. Part of our research focuses on the *size* of the melt pool. However, the melt pool with the same area can have different shapes. For instance, a small circular melt pool and a narrow but elongated melt pool can share the same area. The solid-liquid boundary in such cases differs from each other. The solid-liquid interface affects nucleation as well as grain growth. They, in turn, can alter the final build quality. Thus, the other part of our research targets the *shape* of the melt pool. The shape and size together constitute the complete morphology of the melt pool. Lastly, the repeated heating and cooling of each layer during printing makes the part experience a heat treatment. This thermal history affects the recrystallization and grain transformation phenomena. The thermal history is controlled by the path of the laser. Thus, we consider the *build commands* (consisting of the power and position of the laser) to monitor the shape and size of the melt pool.

Several attempts have been made to identify and understand the parameters affecting the melt pool behaviour. The energy density, ordinarily expressed as a ratio of laser power (P) and velocity (v), is one of the most widely investigated factors affecting the melt pool (Gordon et al. 2020). A low energy density, owing to low laser power or high velocity, accounted for lack-of-fusion defects. Gordon et al. have noticed keyhole porosity in case of high energy density. While the ratio P/v expresses linear energy density considering the hatch spacing (h) and layer thickness (t) to be invariable, other forms like surface energy density (P/vh) by considering variable hatch spacing; and volumetric energy density (P/vht) by varying both hatch spacing as well as layer thickness have also been explored (Thijs et al. 2010). Higher scanning speed creates a narrower melt pool, thereby limiting inter-track fusion. High scanning speed results in porosity as well as higher surface roughness (Kempen et al. 2011). On the other hand, low scan speeds result in an unstable melt pool, which translates into higher volumetric porosity in addition to poor surface roughness and distortion (Kamath et al. 2014). High hatch spacing and layer thickness hinder inter-track and inter-layer fusion. Bertoli et al. recognised the limited capacity of energy density to characterise melt pool and advocated to include additional parameters like hatching and material properties. Additionally, laser spot diameter and material properties (Rubenchik, King, and Wu 2018), powder feed rate and temperature of base plate (Ocylok et al. 2014), preheating temperature (Mertens et al. 2018) and nature of inert gas (Zhang, Dembinski, and Coddet 2013), scan pattern (Yang et al."From Scan Strategy to Melt Pool," 2020) have also been known to affect the melt pool geometry.

The primary driver behind modeling melt pool morphology is to maintain a melt pool of constant size despite the variation in the thermal history and the process parameters. Prior work that attempted to model the melt pool morphology in an L-PBF process mostly relied either on physics or statistics. Physics-based models can constitute simple models as in the Wilson-Rosenthal solution (Ramos-Grez and Sen 2019); or multiscale finite element analysis (FEA) models as in Pal et al. (2014); or computational fluid dynamic models (CFD) as in Zhang and Zhang (2019). Simpler physics models trade-off accuracy in terms of computational expense. Contrarily, although CFD and FEA models are accurate, they are computationally expensive to allow real-time monitoring (Cao et al. 2021). The mesh size in FEA models are usually kept smaller than the beam radius to improve accuracy. Moreover, mesh number increases highly as the build size and the number of laser scan tracks increase.

Adaptive mesh refinement is one of the techniques to improve accuracy with optimal computational complexity. Other high fidelity models can become intractable as the melt pool geometry is directly/indirectly affected by more than 130 parameters (Yadroitsau 2008). Thus, we have chosen machine learning (ML) techniques to facilitate real-time prediction of melt pool *size* as well as *shape*. Employing ML models eliminates the need to solve complex equations based on process understanding (Liu et al. 2020). More importantly, as the melt pool is monitored by capturing its images and deep learning techniques have the best accuracy in image processing (e.g. feature recognition Zhang, Jaiswal, and Rai 2018, inspection Rai and Jaiswal 2021; Yang et al."CNN-LSTM Deep Learning Architecture," 2020), it is a prudent choice to use machine learning to monitor the melt pool from its images.

Several works leveraged machine learning techniques in various facets of additive manufacturing (Sharma, Zhang, and Rai 2021). They are not just limited to process optimisation (Aoyagi et al. 2019), process monitoring (Shevchik et al. 2018), anomaly detection (Scime and Beuth 2018b, 2018a), and monitoring defect artifacts like porosity (Zhang, Liu, and Shin 2019). A few prior research works are related to the prediction of melt pool morphology using machine learning. A shallow neural network with only one hidden layer was used to predict the length and width of the melt pool by considering laser power and speed along with empirical models of the neighbourhood as input parameters (Zhang, Shapiro, and Witherell 2020). A convolutional neural network (CNN) was used to qualitatively classify melt pool images into undermelt, overmelt and regular melt based on the area of the melt pool (Yang et al. 2019). The average width and continuity of the track in an L-PBF process were monitored from videos using CNNs in a semi-supervised setup (Yuan et al. 2019). Akbari et al. used multiple simpler ML models to predict the length, width, and depth from material properties and process parameters. Real-time performance and shape of the melt pool have never been a priority in any of their works.

In the current research endeavour, we adopt the novel objective of predicting the morphology of the melt pool. Unlike previous works (for instance Zhang, Shapiro, and Witherell 2020), we do not limit ourselves to quantifiable attributes of quality like length, width, and depth of the melt pool. In addition to the *area*, we also synthesise the image of the melt pool to predict the *shape* of the melt pool. The shape is a crucial factor that reflects the solid-liquid interface and consequently controls the solidification process. Moreover, we are the first to leverage the instantaneous variables of the process, specifically the *build commands* (consisting of laser power and position), to predict the size and shape of the melt pool. In doing so, we digress from the existing research as they mainly focused on predefined process parameters which remain invariable during the process or are not monitored during the process. One of our input parameters, the *laser position* (in terms of x and y coordinates), is the parameter that offers the maximum variability due to interference (e.g. vibrations) during the process (Stanisavljevic et al. 2020). Incorporating laser position as a parameter captures the spatial variables of the melting and solidification process. Lastly, most of the prior work (like that by Yang et al. 2019 or by Zhang, Shapiro, and Witherell 2020) starts from the images of the melt pool to characterise the melt pool or for feature extraction. That does not support real-time monitoring of melt pool morphology. As we start from the build commands to predict the morphology of the melt pool, our work facilitates real-time monitoring.

We showcase practicable results in predicting the size and shape of the melt pool. We innovate in two aspects to get effective results.

Firstly, We utilise state-of-the-art machine learning models to effectively capture the interdependencies among the respective features of the data samples. We use *long short term memory* (LSTM) networks to predict the area of the melt pool. The architectures of prior work (for example, the PI-LSTM by Singh et al. 2019) are known to be effective at capturing the underlying dependencies among the features of the sample data. The LSTM cells have been used for our specific application to reiterate the processing of the previous features while taking new features as input. This ensures the conditional interdependencies among the features of the data by invoking the memory retention capabilities of the LSTM cell and their recurrent processing ability. This aids the LSTM model to thoroughly process the input features, such as the power, velocity, and density, to predict the melt pool size, which in itself is a function of the interdependencies among these features. Secondly, we use a melt-pool monitoring generative adversarial network (MP-GAN) to synthesise the images of the melt pool to study their shape. This MP-GAN is inspired by the Conditional GAN (cGAN) architecture. To the best of our knowledge, we are the first to predict the shape of the melt pool. Both proposed networks show promising results on experimental data. Figure 1 illustrates our overall computational framework.

The remainder of this paper is organised as follows. Section 2 introduces the data collection, pre-processing and management processes. Section 3 details the LSTM architecture to predict melt pool size, and corresponding results. Section 4 deliberates the melt pool GAN (MP-GAN) for predicting the shape of the melt pool and its

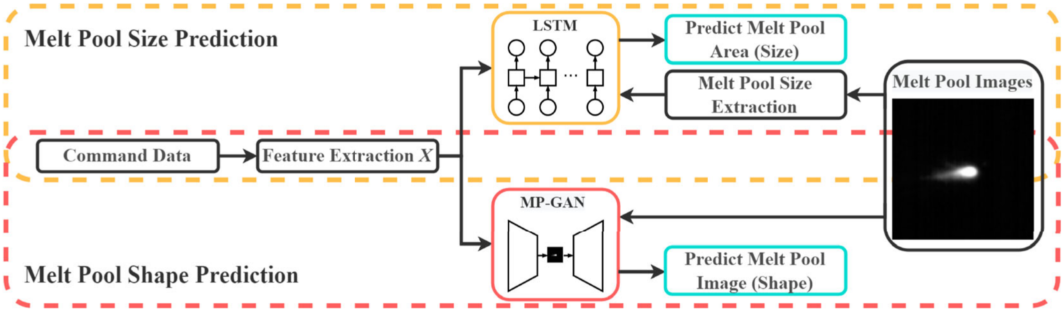

Figure 1. Overall framework for machine learning based prediction of the size and shape of the melt pool.

results. The results are analysed in Section 5. Section 6 ends with concluding remarks.

2. Experiment setup

2.1. Data collection

The experiment is conducted on the National Institute of Standards and Technology (NIST) Additive Manufacturing Metrology Testbed (AMMT) (Lane et al. 2016). The NIST AMMT is a fully custom, open-platform L-BPF system to advance the research on control, monitoring, and metrology. The in-house developed AM control software (SAM) allows the creation of various scan strategies from a simple combination of different scan paths and laser power/speed control (Yeung et al. 2018). The melt pool incandescent emission is diverted to a high-speed camera by a dichroic mirror and filtered at a bandwidth of $(85 + / - 20)$ nm. The custom optics enable 1:1 magnification and an image resolution of 8 μm. The laser position triggers the camera so that the melt pool monitoring (MP) image can be precisely mapped to its location.

The experiment on AMMT builds four 3D parts with the same geometry: $5\,\text{mm} \times 9\,\text{mm} \times 5\,\text{mm}$. The parts were built on a wrought nickel alloy 625 (IN625) substrate cut to $100\,\text{mm} \times 100\,\text{mm} \times 12.5\,\text{mm}$. AMMT deploys a stripe pattern with overshooting strategy to scan the entire part. This experiment collects two types of data: command data and coaxial melt pool image. The command data consists of the location of the laser (x, y), and the power of the laser (P). The coaxial melt pool images are grayscale images of $120\,\textit{pixel} \times 120\,\textit{pixel}$ size. Each pixel corresponds to an area of $8\mu\text{m} \times 8\mu\text{m}$.

As mentioned earlier, we have two tasks in this research: (1) melt pool prediction and (2) melt pool generation. A total of 17,692 data samples are collected, out of which 11742 samples are used for training, and 5950 for testing. The training samples are collected from three parts, and testing samples are collected from an individual part. Each data sample pair includes command data and a coaxial melt pool image. In the melt pool prediction task, the command data is served as the input, and the output (melt pool size) is extracted from the melt pool image. In the melt pool generation task, the melt pool image is applied as real samples, and the command data is regarded as the conditions of the generation network. Before infusing the data into the model, the data is preprocessed for noise removal.

2.2. Data preprocessing

2.2.1. Melt pool size extraction

The coaxial melt pool images are represented as a grayscale ranging from 0 to 255. The pixel value is directly proportional to the temperature (Lane and Yeung 2020). It must be noted that the grayscale saturates as the temperature exceeds 2100 °C. In the experiment, some bad data samples are removed which are caused by preheating of the camera. Then, a threshold method is applied to extract the melt pools. This study chooses 80 as the threshold value, which has been shown to make the extracted melt pool size consistent with manual measurement and has been verified in previous research (Lane and Yeung 2020; Yeung, Yang, and Yan 2020; Yang et al."3D Build Melt Pool Predictive Modeling," 2020).

Nonetheless, the noise observed in the melt pool images of an L-PBF process is potentially a pernicious phenomenon (Criales et al. 2017). When the laser beam strikes the metallic powder, local evaporation ejects minute melt pool particles and blows away surrounding heated particles due to the strong local convective flow. These ejected and blown particles induce spatter. Spattering particles originate from the vicinity of the melt pool. Therefore, they have high temperatures and thus appear as bright clusters of pixels (Khairallah et al. 2016) (as shown in Figure 2(a)). Besides, in some of the premelted areas, the material's temperature elevates rapidly, which results in a bright region. Both cases will interfere with the coaxial melt pool images, affecting the ground truth estimation of the melt pool.

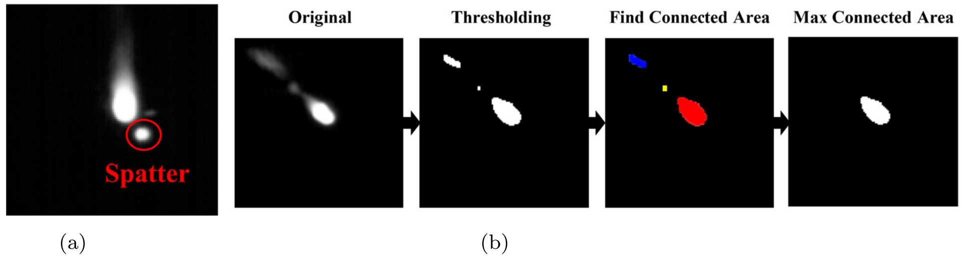

Figure 2. Denoising of melt pool Image. (a) Spatter and (b) melt pool extraction.

Table 1. Encoded direction (v_d) of the velocity vector.

Velocity Angle	$[-\frac{\pi}{4}, \frac{\pi}{4})$	$[\frac{\pi}{4}, \frac{3\pi}{4})$	$(-\frac{3\pi}{4}, -\frac{\pi}{4}]$	$[\frac{3\pi}{4}, \pi]$ or $[-\pi, -\frac{3\pi}{4}]$
v_d	0	1	2	3

To mitigate the adversities mentioned above, we employ a noise removal method to improve the accuracy of the extracted size of the melt pool. Figure 2(b) shows the melt pool extraction procedure. We use the threshold of 80 to extract the high-temperature area. Then, we separate all the connected areas by inspecting their Moore Neighborhood (Weisstein 2005). Only the maximum connected area is selected as the melt pool. The melt pool size is calculated by counting the pixels in that area. Finally, the melt pool size (s) is converted to real measurement by using $S = s * 6.4\,\mathrm{e}^{-5}$, where S is the melt pool area in the real scale (mm^2) and s is the melt pool area in pixels (Lane et al. 2016).

2.2.2. Feature extraction

The build command data (x, y, P) is preprocessed to extract more useful information to boost the performance of our network. Prior research identified the substantial impact of laser velocity and power density on melt pool formation. Yang et al."From Scan Strategy to Melt Pool," (2020), Lu et al. (2018) and Thijs et al. (2010). Therefore, we include the velocity of the laser (v) by calculating it using the central difference method. Besides the magnitude of the velocity, the direction of the velocity vector is encoded into a discrete value (v_d). It is represented by four classes (as shown in Table 1). The laser power density is computed by using $d = P/v$. Finally, a vector that includes (x, y, P, v, v_d, d) at each step becomes the inputs of the prediction network and the conditions of the generation network.

2.3. Computational resources

All the training and testing procedures are executed using Tensorflow on a server with Linux Centos 7.5.x operation system, Intel Xeon Gold 6230 processor (40 cores @2.10GHz), 32GB RAM, and NVIDIA Tesla V100 GPU.

3. Melt pool size prediction

3.1. LSTM

LSTM (Hochreiter and Schmidhuber 1997), a kind of Recurrent Neural Network, was designed to model the dynamic systems' temporal dependencies. In the past, LSTMs have been successfully applied to sequential data processing and time series forecasting. Besides, the LSTMs are used for the tasks of speech recognition (Petridis, Li, and Pantic 2017) and language modeling. Herein, we used an LSTM-based data-driven model for predicting the area (*size*) of the melt pool. Inspired by one of our previous works (Singh et al. 2019), we innovatively use the sensor data by exploiting the memory retention capabilities and recurrent processing power of the LSTM units. As opposed to simply depending on the time-series reliance of the datasets, similar to the conventional approach, we feed the dataset features to different timesteps of the LSTM unit. In the process, we put an end to the dependency of LSTM cells on sequential data. Our model, as shown in Figure 3(a), has LSTM cells with six (same as the number of features in the training data) time (or recurrent processing) steps. The network's input is X that contains (x, y, P, v, v_d, d), and the output Y_r is the size of the melt pool area. The approach, as mentioned above, makes sure that we invoke the rigorous data processing power of the memory cells.

Figure 3(b)) demonstrates the working of the individual LSTM cell. x_t is the input feature at time step t, and a^t is the hidden activation at time step t, represented by Equation (3). The internal state c^t is determined using Equation (2). $c^{\sim t}$, determined using Equation (1), works as a placeholder for c^t. At time step t, c^t is obtained using c^{t-1} and $c^{\sim t}$.

$$c^{\sim t} = \tanh(W_a^c a^{t-1} + W_x^c x_t) \quad (1)$$

$$c^t = f^t \bigotimes c^{t-1} + u^t \bigotimes c^{\sim t} \quad (2)$$

$$a^t = o^t \bigotimes \tanh(c^t). \quad (3)$$

Here, W_j^i denotes the weight matrices. f^t, u^t, and o^t are the forget gate, update gate, and output gate, respectively

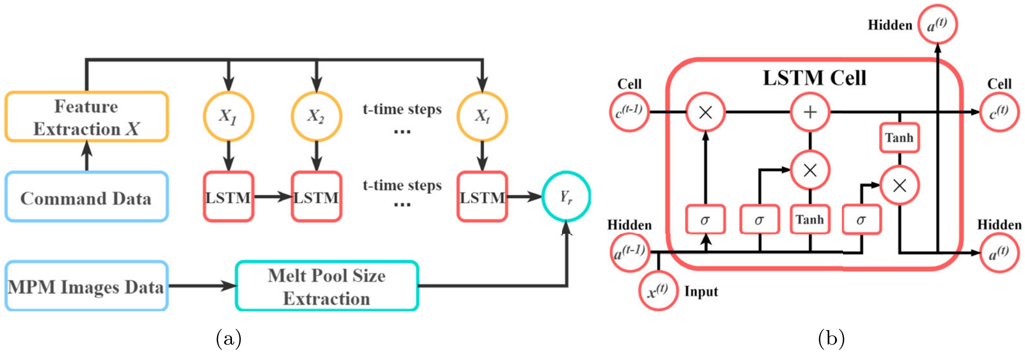

Figure 3. LSTM Network. (a) LSTM Network Architecture and (b) LSTM Cell.

and are calculated as follows:

$$f^t = \sigma(W_a^f a^{t-1} + W_x^f x_t) \tag{4}$$

$$u^t = \sigma(W_a^u a^{t-1} + W_x^u x_t) \tag{5}$$

$$o^t = \sigma(W_a^o a^{t-1} + W_x^o x_t) \tag{6}$$

where, σ is the logistic sigmoid function. a^t is the information accumulated, till time step t, due to the recurrent processing of previous time steps. The final output, which is the melt pool size, is determined using a^t.

3.2. Hyperparameter tuning

The process alludes to choosing a bunch of ideal parameters during the training process, which yields an optimally fitting model for a given dataset (Claesen and De Moor 2015). Typical examples of hyperparameters include layer size, filter size, total layers, batch size, and learning rate. In this paper, we obtain the optimal model configuration by evaluating various combinations of the chosen hyperparameters. The selected hyperparameters are the number of neurons in the LSTM layer, type of optimiser, number of training epochs, and batch size. The algorithm used a grid search over a parameter grid of 72 candidate combinations, with five-fold cross-validation, resulting in 360 fits of the entire training dataset. The best hyperparameter combination culminated into a model that uses a batch size of 100, deploys Adam as the principal optimiser, incorporates five neurons in the LSTM layer, and runs over 200 epochs of training.

3.3. Results and analysis

The devised model registers a mean average error of 0.0024 mm^2 over the testing set. Also, we define the model accuracy as the ratio of the absolute error between the predicted melt pool size and the observed value to the observed melt pool size. Besides, owing to its efficient data handling, the model exhibits a mean accuracy of 90.7 percent on the testing data. To evaluate the impact of the melt pool over the whole part, the contour plot and 3D surface plot are generated (as shown in Figure 8). The value of the z-axis in the 3D surface plot (the colour in the contour plot) represents the size of the melt pool area; the x and y-axis are the coordinates of the laser point. The closed square is the manufactured part. As depicted from Figure 8, the overall distribution of ground truth and the predicted melt pool size are similar. Moreover, the large melt pools in the predicted results are accurately captured, which can help to optimise the manufacturing procedure. We compared various deep learning architectures for predicting the melt pool size, and the results are enumerated in Table 2. It is patent from the tabular data that the LSTM outperforms the other two types of model architectures to predict the melt pool area.

Table 2. Model comparison.

Model	DNN	GRU	LSTM
Trainable Parameters	651	826	146
Number of Layers	3	2	2
Optimizer	RMSprop	Adam	Adam
Batch Size	200	50	100
Training Epoch	500	100	200
MAE (mm^2)	0.0030	0.0033	0.0024
Accuracy (%)	89.9	88	90.7

4. Melt pool image generation

4.1. MP-GAN

In the previous section, we predicted the *size* of the melt pool by using an LSTM network. However, focusing only on the melt pool *size* does not offer any information about the geometry of the melt pool. The geometry, in terms of the *shape* of the melt pool, can provide additional insight into the manufacturing process. For instance, the melt pool can develop a long tail if the velocity is high. The high velocity may not melt the powder particles properly and thus could be detrimental to the fusion process. That will create lack-of-fusion pores. On the other hand, a melt pool with a uniform but large shape can arise due to a relatively slower velocity. This case is favourable for keyhole porosity. Hence, realising the gravity of the shape of the melt pool, we propose a melt pool GAN (MP-GAN) to generate the melt pool images to obtain more comprehensive information about the melt pool. Our MP-GAN is inspired by conditional Generative Adversarial Network (cGAN) (Mirza and Osindero 2014). The proposed model consists of two networks: a generator $G(z, c_c, c_d; \theta_g)$ and a discriminator $D(s, c_c, c_d; \theta_d)$, where z is the input noise vector, s is either the ground truth or synthetic melt pool image, c_c is the continuous conditional vector, c_d is the discrete conditional vector, and θ_g and θ_d are the training parameters within generator and discriminator respectively. For the melt pool generation problem, the continuous condition vector c_c includes laser position (x, y), power (P), power density (d) and magnitude of velocity (v). The discrete conditional vector c_d only contains direction of the velocity vector (v_d).

4.1.1. Network architecture

- Generator: Our purpose is to generate melt pool images based on the previously generated feature vector. A generator that can learn the combining distribution of feature vectors and given real melt pool images is needed. Therefore, we constructed a generator based on a deconvolution network. As shown in Figure 4, the inputs to the generator are the noise vector z and the conditional vector c. As we discussed previously, we have two types of conditional vectors: continuous condition c_c and discrete condition c_d. Two conditional inputs are embedded into the shape of $10 \times 10 \times 1$, and noise input is embedded into $10 \times 10 \times 128$ before concatenating together. Thus, z and c are embedded as joint hidden representation h in a high dimensional space. Finally, a three-layer deconvolution neural network is utilised to generate the melt pool image from the hidden vector h. The detail of the architecture is described in Table 3.
- Discriminator: To evaluate the quality of the synthetic image, we design a CNN to perform the classification task. Similar to the generator, the two conditional inputs of the discriminator are embedded into a shape of $120 \times 120 \times 1$ individually, and they are concatenated with the input images ($120 \times 120 \times 1$). The embedded vector is then infused into the two-layered CNN to perform a 'Real/Fake' classification. The architecture parameters can be found in Table 3.

4.1.2. Loss function

The objective of the original GAN can be regarded as a minimax assignment where the generator (G) tries to minimise this objective while the discriminator (D) attempts to maximise it according to the following expression:

$$\min_G \max_D L(D, G) = \mathbb{E}_{x \sim p_d(x)} \log D(x) + \mathbb{E}_{z \sim p_z(z)} \log(1 - D(G(z))) \tag{7}$$

where G builds a mapping relation from the noise distribution $p_z(z)$ to the distribution $p_d(x)$ and D evaluates the probability that a sample originates from the distribution $p_d(x)$ rather than from the generator G (Mirza and Osindero 2014; Liao et al. 2019). In our MP-GAN, the conditional information c_c and c_d are added to G and D so that G can capture the data distribution based on conditions. Besides, D also takes conditional information to make sure the generated images are able to follow the distribution. Thus, the objective function of MP-GAN is as follows:

$$\begin{aligned}\min_G \max_D L(D, G) &= \mathbb{E}_{x \sim p_d(x)} \log D(x, c_c, c_d) \\ &\quad + \mathbb{E}_{z \sim p_z(z)} \log(1 - D(G(z, c_c, c_d)))\end{aligned} \tag{8}$$

4.2. Results and analysis

4.2.1. Training procedure

The procedure of training the proposed MP-GAN is shown in Algorithm 1. To prevent saturation, we update the discriminator three times in every iteration ($k = 3$). Besides, we also apply dropout in D after flattening to avoid overfitting. Based on our computational resources, the minibatch size (m) is set to 150. In addition, the Adam optimiser, with a learning rate of 0.0002, is utilised to optimise the Binary Cross Entropy loss for training both G and D. The total training time is 7 h 16 min for 50 epochs.

4.2.2. Qualitative evaluation

We train our MP-GAN for 50 epochs. The evolution of the generator's result is shown in Figure 5. Several combinations of conditional parameters are selected as inputs. After each epoch, the generator synthesises the corresponding images. As depicted in Figure 5, first, the generator tries to learn the melt pool position. Then the generator learns to generate the smooth boundary of the melt pool. Finally, after sufficient epochs of training, the generator is able to capture the intricate details of the melt pool. By comparing the synthetic results with ground truth (GT), it is evident that the generator is able to synthesise the melt pool images with high precision and accuracy.

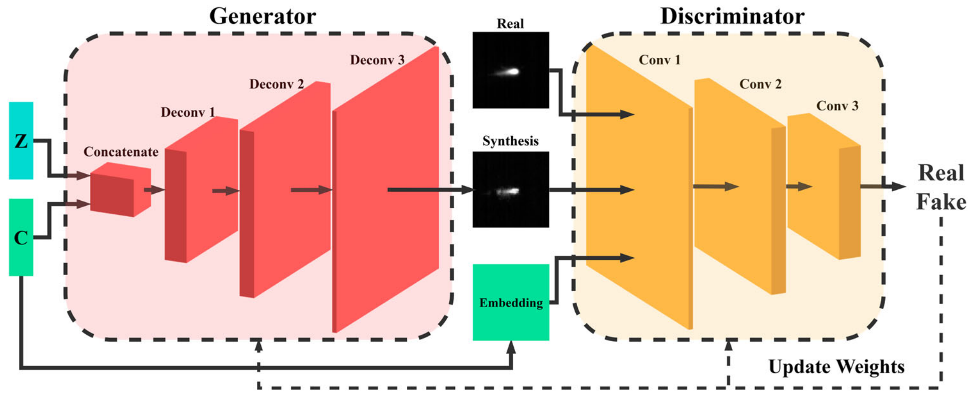

Figure 4. MP-GAN architecture.

Table 3. MP-GAN hyper architecture.

	Layer	Filter Size	Number Filters	Stride	Padding	Activation	Output Shape
G	Deconv1	4 × 4	128	(3, 3)	'Same'	LeakyReLU	(30, 30,128)
	Deconv2	3 × 3	128	(2, 2)	'Same'	LeakyReLU	(60, 60, 128)
	Deconv3	2 × 2	128	(2, 2)	'Same'	LeakyReLU	(120,120,128)
D	Conv1	4 × 4	128	(2, 2)	'Same'	LeakyReLU	(60, 60, 128)
	Conv2	3 × 3	128	(2, 2)	'Same'	LeakyReLU	(30,30,128)
	Flatten	–	–			–	(115200,1)

After comparing all synthetic images and ground truth images, we observed a few exceptional cases. As shown in Figure 6, we can notice some spatters and abnormal melt pools in the ground truth images. However, the synthesised images are not able to obtain these abnormal behaviours. Since the neural network is robust to the noise, the spatter and abnormal regions vanish during training.

4.2.3. Quantitative evaluation

- *Melt pool size*: After getting the synthetic melt pool images, we first verified if the synthetic melt pool images could provide an accurate estimate of the melt pool size. By applying thresholding and pixel counting methods discussed in Section 2.2, we compared the size of the melt pool in synthetic images with those of ground truth images. The mean absolute error

---

Algorithm 1 Minibatch stochastic gradient descent training of MP-GAN (Goodfellow et al. 2014).

Require: The number of steps applied to the discriminator k; the parameters of generator and discriminator θ_g and θ_d; the batch size m and the number of training iterations n.

for n **do**
  for k steps **do**
    Sample a minibatch of m noise samples from the noise prior $p_g(z)$.
    Sample minibatch of m examples from training melt pool images x.
    Extract the corresponding conditional parameters from c_c and c_d.
    Update the discriminator by ascending its stochastic gradient:

$$\nabla_{\theta_d} \frac{1}{m} \sum_{i=1}^{m} \left[\log D\left(x^{(i)}, c_c^{(i)}, c_d^{(i)}\right) + \log\left(1 - D\left(G\left(z^{(i)}, c_c^{(i)}, c_d^{(i)}\right)\right)\right)\right]$$

  end for
  Sample a minibatch of m noise samples from noise prior $p_g(z)$.
  Update the generator by descending its stochastic gradient:

$$\nabla_{\theta_g} \frac{1}{m} \sum_{i=1}^{m} \log\left(1 - D\left(G\left(z^{(i)}, c_c^{(i)}, c_d^{(i)}\right)\right)\right)$$

end for

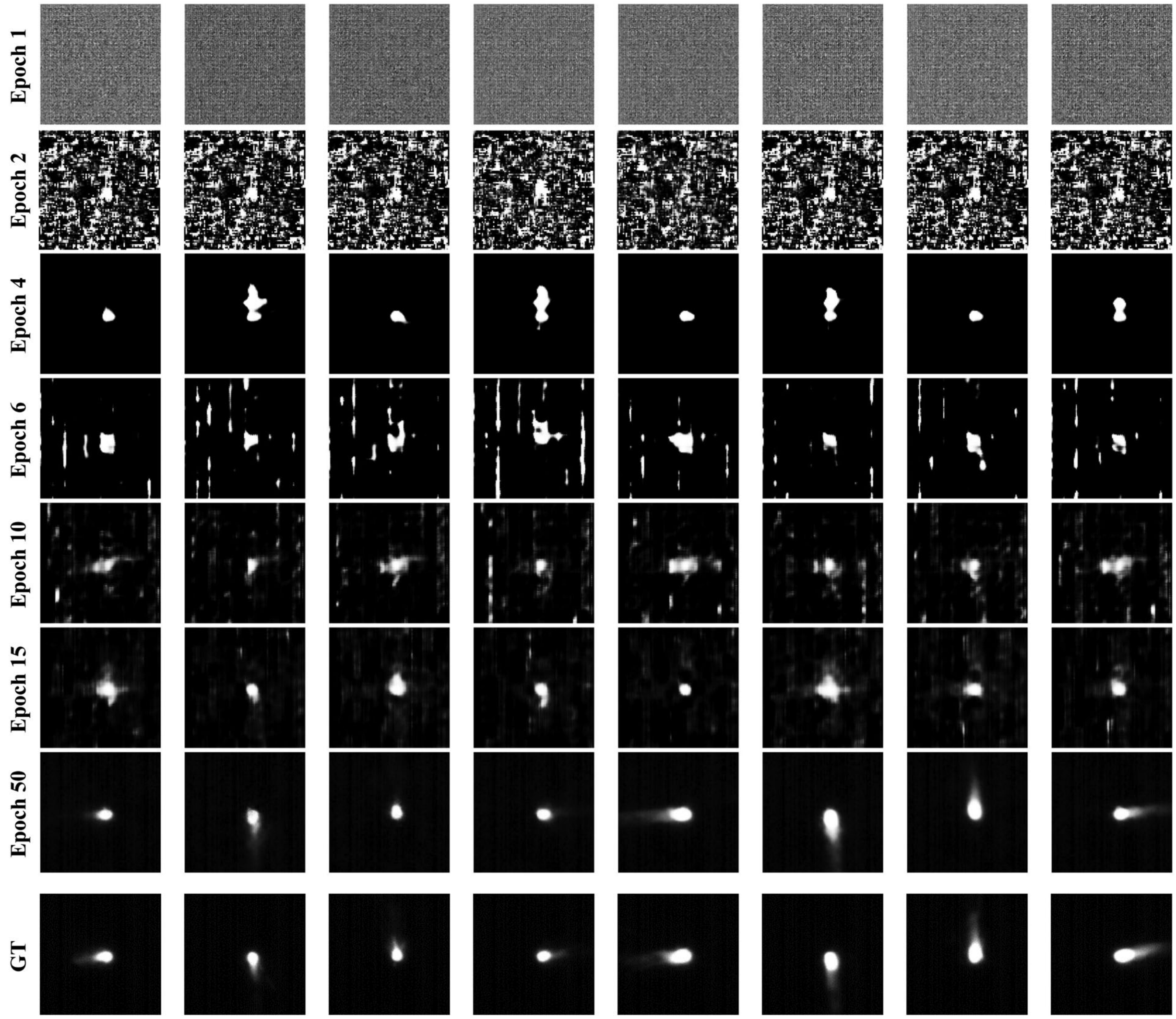

Figure 5. Examples of MP-GAN training procedure through training epochs. **GT** is Ground Truth.

(MAE) of melt pool size is 0.0029 mm^2, and the accuracy is 88.7%. We also looked into the global performance of the melt pool size, shown in Figure 8. The contour plot and 3D surface of the melt pool size illustrate that the synthetic melt pool images follow the overall distribution of ground truth. While MP-GAN is less accurate than the melt pool prediction network, MP-GAN still achieves a satisfactory performance. The additional error mainly arises from two factors. (1) GANs themselves are not stable enough to perform regression problems. (2) The raw image is directly used to train the generator. Presence of spatter and plume in the ground truth data accounts for this error.

- *Melt pool shape*: Generating synthetic images of the melt pool offers more flexibility in analysing the properties of the melt pool than only predicting its size. Hence, we also investigated if the shapes of generated melt pool images follow those of the ground truth images. Since the melt pool's shape resembles an ellipse, a least-square ellipse regression method is applied to find the bounding ellipses (Gander, Golub, and Strebel 1994). Additionally, similar to melt pool size calculation, we use 80 as a threshold to extract the melt pool boundary at the beginning of the processing. The processing steps are illustrated in Figure 7. As shown in the figure, the blue contour is the melt pool boundary after the threshold method, and the red contour is the ellipse extracted by regression. Finally, the length of the ellipse's major and minor axes and rotation angle are considered as the characteristics to evaluate the synthetic images. The results (displayed in Table 4) demonstrate that prediction accuracy is satisfactory. However, it is lower than that of the melt pool size due to the error in the ellipse regression method.
- *SSIM*: Structural similarity (SSIM) is used for measuring the similarity between two images. SSIM is based on three comparison metrics between the ground

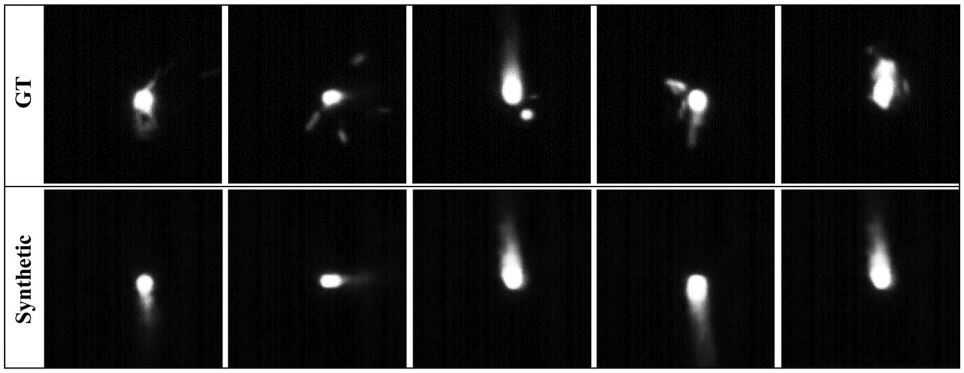

Figure 6. Abnormal results.

truth image x and synthetic image y: luminance $l(x,y)$, contrast $c(x,y)$ and structure $s(x,y)$ (Wang, Simoncelli, and Bovik 2003). They are expressed as:

$$l(x,y) = \frac{2\mu_x\mu_y + c_1}{\mu_x^2 + \mu_y^2 + c_1} \quad (9)$$

$$c(x,y) = \frac{2\sigma_x\sigma_y + c_2}{\sigma_x^2 + \sigma_y^2 + c_2} \quad (10)$$

$$s(x,y) = \frac{\sigma_{xy} + c_3}{\sigma_x\sigma_y + c_3} \quad (11)$$

where $\mu_x, \mu_y, \sigma_x, \sigma_y, \sigma_{xy}$ are average, variance and covariance respect to $x$and$y$; c_i is constant. The SSIM can be calculated by:

$$SSIM(x,y) = l(x,y)c(x,y)s(x,y) = \frac{\left(2\mu_x\mu_y + c_1\right)\left(2\sigma_{xy} + c_2\right)}{\left(\mu_x^2 + \mu_y^2 + c_1\right)\left(\sigma_x^2 + \sigma_y^2 + c_2\right)} \quad (12)$$

The SSIM value of our test set is 0.91, indicating that the synthetic images are indeed close to the ground truth.

- *PSNR*: The peak signal-to-noise ratio (PSNR) is widely used to measure the quality of generation (Salomon 2004; Wolterink et al. 2017). It is an approximation to human perception of the quality of image generation. The first step is to find the mean square error (MSE) between two images x and y:

$$MSE_{x,y} = \frac{1}{mn}\sum_{i=0}^{m-1}\sum_{j=0}^{n-1}[x(i,j) - y(i,j)]^2 \quad (13)$$

Then the PSNR value of x and y can be represented as:

$$PSNR_{x,y} = 10\log_{10}\left(\frac{MAX_x^2}{MSE_{x,y}}\right) \quad (14)$$

in which, MAX_x is the maximum possible pixel intensity ($= 255$). The PSNR value of the synthesised images of the test data is 32.34 dB, which reflects our model's promising performance.

Table 4. Melt pool shape evaluation.

	Major Axis (mm)	Minor Axis (mm)	Rotation Angle (degree)
MAE	0.026	0.008	2.79
Accuracy	92.0%	86.9%	–

5. Discussion

A closer look at the contour plots of the area of the melt pool reveals that the contours generated by the LSTM (Figure 8(e)) and the MP-GAN (Figure 8(f)) are strikingly similar to that of the ground truth data (Figure 8(d)). The $>$ 90% accuracy of the LSTM network and the 0.91 similarity score of the MP-GAN advocate for their usage in real applications. A higher melt pool area obtained from the LSTM network reflects high energy density. It should be lowered proportionately to avoid overmelting and the consequent keyhole porosity. Contrarily, in the case of a low melt pool area that indicates low energy density, the energy density shall be increased to avoid lack-of-fusion pores.

The images generated by the MP-GAN can reduce the reliance on expensive high-speed cameras used to capture the melt pool images during the process. The generated images can offer deeper insights into process control. For instance, the generated images capture the shape of the melt pool in two dimensions. Thus, the melt pool's length and width (major and minor axes) can be inferred from those images. The length of the melt pool can help in controlling the scan velocity. The scan velocity can be lowered if the length is high and vice-versa. Correlating the inferred width with hatch spacing can help in controlling inter-track fusion. If the melt pool width is lower than the hatch spacing, it will hinder fusion between adjacent tracks. The condition becomes

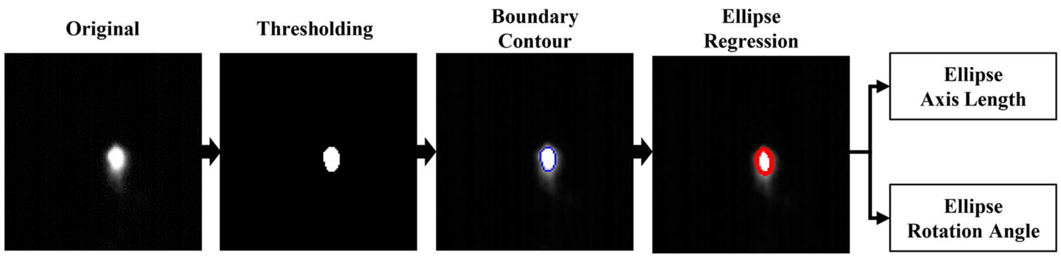

Figure 7. Ellipse regression processing.

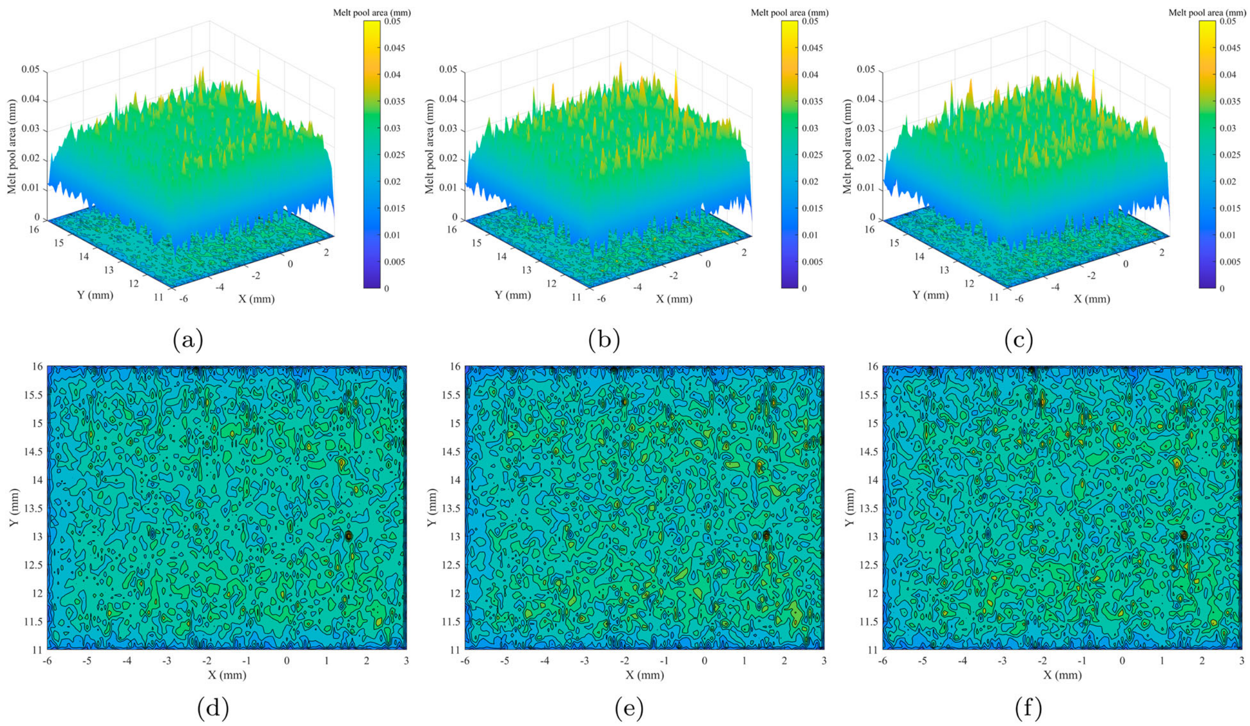

Figure 8. Contour and 3D surface comparison. (a) 3D surface of ground truth. (b) 3D surface of LSTM model. (c) 3D surface of MP-GAN model. (d) Contour plot of ground truth. (e) Contour plot of LSTM model and (f) Contour plot of MP-GAN model.

favourable for balling and lack-of-fusion pores. A higher area and a melt pool width higher than the optimal width signifies high energy density. Increasing the scan velocity or decreasing the laser power can balance the energy density.

The images of the melt pool do not offer any information about the depth of the melt pool. A volumetric rendering of the melt pool can offer significantly more information about the morphology of the melt pool. It can support monitoring of the inter-layer fusion behaviour. Additionally, this research work solicits further investigation to capture the synthesis and disappearance of spatter.

6. Conclusion and future work

In the current research endeavour, the melt pool morphology in a laser-based powder bed fusion additive manufacturing process is predicted from build commands. Two components of the morphology, *size* and *shape*, are predicted using machine learning. The area (size) of the melt pool is predicted using an *LSTM* network. The *shape* is inferred by synthesising the images of the melt pool using a *melt pool GAN* (MP-GAN). The LSTM network achieved an accuracy of 90.7% in estimating the area of the melt pool. The MP-GAN could generate the melt pool images with satisfactory precision and accuracy. A structural similarity score of 0.91 of the synthesised images on the test data demonstrates the efficacy of our approach. Our method can enable real-time monitoring and feedback control at the layer level, thereby improving final build quality. Additionally, the high-frequency melt pool image synthesis can reduce the reliance on sophisticated instrumentation. The AM process can also be optimised by simulating it prior to execution.

The investigation can be further advanced in multiple directions, including the manufacturing process as well as modeling. Parts with complex geometry and variations in process parameters can be promising avenues for future research. The models can also be improved using different architectures and physics-guided neural networks.

Acknowledgements

The views and conclusions contained in this document are those of the authors and should not be interpreted as representing the official policies, either expressed or implied, of the Army Research Laboratory, or the U.S. Government. The U.S. Government is authorised to reproduce and distribute reprints for Government purposes notwithstanding any copyright notation herein. We also thank Brandon Lane (Mechanical Engineer, NIST) for generating and providing the melt pool data sets for our experiment.

Data availability statement

The data that support the findings of this study are available from the corresponding author, RR, upon reasonable request.

Disclosure statement

No potential conflict of interest was reported by the author(s).

Funding

This research was sponsored by the Army Research Laboratory and was accomplished under Cooperative Agreement Number W911NF2020237.

Notes on contributors

Zhibo Zhang, currently a research scientist at KLA, holds a Ph.D. degree in Mechanical Engineering from the University at Buffalo, SUNY, which he received in 2021. He also obtained an M.S. degree in Mechanical Engineering from the same institution in 2017. Before moving to the USA, he worked as a mechanical engineer in China. Zhang's research interests cover a broad range of areas, including machine learning, hybrid modeling, intelligent manufacturing, and image processing. Presently, he is focused on investigating the intersection of physics and machine learning.

Chandan Kumar Sahu is currently pursuing his Ph.D. degree in automotive engineering at Clemson University. He received his bachelors from National Institute of Technology Rourkela, India, in 2014, and his masters from the State University of New York at Buffalo, USA, in 2020, both in mechanical engineering. He led the homologation of the development of new models at Honda Motorcycle and Scooter India from 2014 to 2017.
He is interested in machine learning in general, with a focus on its geometric attributes and mechanical applications. His research investigated additive manufacturing, augmented reality, cyber-physical systems, and engineering design applications using computational tools like machine learning, graph theory, and natural language processing. His current research aspires to develop mathematical models of requirements to capture their interrelationships to investigate the role of requirements during the evolution of a system.

Shubhendu Kumar Singh received a B.E. degree, in Mechanical Engineering, from the Birla Institute of Technology, Mesra, Ranchi, India, in 2014 and an M.S. degree in Mechanical Engineering from the State University of New York at Buffalo, USA, in 2019. He is pursuing his Doctoral Degree in Automotive Engineering from Clemson University, USA. He has worked as an Engineer at Tractors and Farm Equipment Limited (TAFE Ltd.), India. Part of his job responsibilities at TAFE Ltd. involved solving technical and operational issues related to the tractors. Specifically, the problems related to the Powertrain (Engine, Turbocharger) and Transmission system. He has also worked as a Machine Learning intern at the Los Alamos National Lab, USA. He is a Research Assistant at Geometric Reasoning and Artificial Intelligence Laboratory (GRAIL) at Clemson University.
In recent years, he has worked on various projects at the intersection of Artificial Intelligence and Engineering. A few of these projects have been supported by DARPA, ONR, and CESMII. His current research endeavours are focused on Artificial Intelligence, Computer Vision, Physics-Informed Machine Learning and their application in Design-Manufacturing, Fault Diagnostics and Prognostics, and Cyber-Physical Systems.

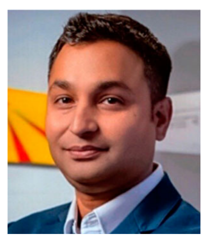

Rahul Rai joined the Department of Automotive Engineering in 2020 as Dean's Distinguished Professor in the Clemson University International Center for Automotive Research (CU-ICAR). He also holds appointments in the Computer Science and Mechanical Engineering departments at Clemson University. He is Associate Director of Artificial Intelligence Research Institute in Science and Engineering (AIRISE) at Clemson University. He directs the Geometric Reasoning and Artificial Intelligence Lab (GRAIL, which is located at both CU-ICAR and Center for Manufacturing Innovation (CMI). Previously, he served on the Mechanical and Aerospace Engineering faculty at the University at Buffalo-SUNY (2012–2020). Dr. Rai also has industrial research centre experiences at United Technology Research Center (UTRC) and Palo Alto Research Center (PARC). Dr. Rai received his B.Tech. degree in 2000 and M.S. degree in 2002 in Manufacturing Engineering from the National Institute of Foundry and Forge Technology (NIFFT), Ranchi, India, and Missouri University of Science and Technology (Missouri S&T) USA, respectively. He earned his doctoral degree in Mechanical Engineering from The University of Texas at Austin USA in 2006.
Dr. Rai's research is focused on developing computational tools for Manufacturing, Cyber-Physical System (CPS) Design, Autonomy, Collaborative Human-Technology Systems, Diagnostics and Prognostics, and Extended Reality (XR) domains. By combining engineering innovations with methods from machine learning, AI, statistics and optimisation, and geometric

reasoning, his research strives to solve important problems in the above-mentioned domains. His research has been supported by NSF, DARPA, ONR, ARL, NSWC, DMDII, CESMII, HP, NYSERDA, and NYSPII (funding totalling more than $20M as PI/Co-PI). He has authored over 100 papers to date in peer-reviewed conferences and journals covering a wide array of problems. Dr. Rai is the recipient of numerous awards, including the 2009 HP Design Innovation, 2017 ASME IDETC/CIE Young Engineer Award, and 2019 PHM society conference best paper award. Additionally, Dr. Rai is Associate Editor of the International Journal of Production Research and ASME Journal of Computing and Information Science in Engineering (JCISE) journals and has taken significant leadership roles within the ASME Computers and Information in Engineering professional society.

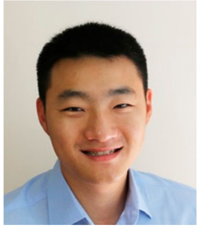

Zhuo Yang is a research associate at National Institute of Standards and Technology (NIST). He received a Ph.D. degree in Mechanical Engineering from University of Massachusetts Amherst in 2018. His bachelor degree was in Mechanical Engineering from Beijing University of Technology in 2009. He was a mechanical engineer in Beijing Wandong Medical from 2009–2012, mainly focusing on developing radiology equipment such as CT and MRI.
His current research interests include Additive Manufacturing, design optimisation, machine learning, and real-time control. His current project is about data fusion and registration in powder bed fusion additive manufacturing.

Yan Lu Dr. is a member of the System Integration Division at the Engineering Lab. Her research interests at NIST include additive manufacturing data registration, data integration and fusion, and smart manufacturing system information modeling and integration architecture.
Before joining NIST, Dr. Lu was the head of Grid Automation and Production Operation and Optimization Research Group at Siemens Corporation, Corporate Technology. With Siemens, she has led and successfully delivered tens of million dollars of corporate funded and government funded research projects in the areas of survivable control systems, energy automation and building energy management systems. She has published more than 100 peer reviewed journal and conference papers and was granted more than 15 patents in industry and building automation technology. Dr. Lu also worked for Seagate Research Center for two years on developing hard disk drive servo control.

ORCID

Zhibo Zhang http://orcid.org/0000-0001-9293-2187
Chandan Kumar Sahu http://orcid.org/0000-0001-5893-4031
Rahul Rai http://orcid.org/0000-0002-6478-4065

References

Akbari, Parand, Francis Ogoke, Ning-Yu Kao, Kazem Meidani, Chun-Yu Yeh, William Lee, and Amir Barati Farimani. 2022. "MeltpoolNet: Melt Pool Characteristic Prediction in Metal Additive Manufacturing Using Machine Learning." *Additive Manufacturing* 55: Artlcle ID 102817. doi:10.1016/j.addma.2022.102817.

Aoyagi, Kenta, Hao Wang, Hideki Sudo, and Akihiko Chiba. 2019. "Simple Method to Construct Process Maps for Additive Manufacturing Using a Support Vector Machine." *Additive Manufacturing* 27: 353–362. doi:10.1016/j.addma.2019.03.013.

Bertoli, Umberto Scipioni, Alexander J. Wolfer, Manyalibo J. Matthews, Jean-Pierre R. Delplanque, and Julie M. Schoenung. 2017. "On the Limitations of Volumetric Energy Density as a Design Parameter for Selective Laser Melting." *Materials & Design* 113: 331–340. doi:10.1016/j.matdes.2016.10.037.

Cao, Yang, Xin Lin, Nan Kang, Liang Ma, Lei Wei, Min Zheng, Jun Yu, Dongjian Peng, and Weidong Huang. 2021. "A Novel High-Efficient Finite Element Analysis Method of Powder Bed Fusion Additive Manufacturing." *Additive Manufacturing* 46: Artlcle ID 102187. doi:10.1016/j.addma.2021.102187.

Claesen, Marc, and Bart De Moor. 2015. "Hyperparameter Search in Machine Learning." *arXiv preprint arXiv:1502.02127*.

Criales, Luis E., Yiğit M. Arısoy, Brandon Lane, Shawn Moylan, Alkan Donmez, and Tuğrul Özel. 2017. "Laser Powder Bed Fusion of Nickel Alloy 625: Experimental Investigations of Effects of Process Parameters on Melt Pool Size and Shape with Spatter Analysis." *International Journal of Machine Tools and Manufacture* 121: 22–36. doi:10.1016/j.ijmachtools.2017.03.004.

Dilip, J. J. S., Shanshan Zhang, Chong Teng, Kai Zeng, Chris Robinson, Deepankar Pal, and Brent Stucker. 2017. "Influence of Processing Parameters on the Evolution of Melt Pool, Porosity, and Microstructures in Ti-6Al-4V Alloy Parts Fabricated by Selective Laser Melting." *Progress in Additive Manufacturing* 2 (3): 157–167. doi:10.1007/s40964-017-0030-2.

Gander, Walter, Gene H. Golub, and Rolf Strebel. 1994. "Least-squares Fitting of Circles and Ellipses." *BIT Numerical Mathematics* 34 (4): 558–578. doi:10.1007/BF01934268.

Ghiasian, Seyedeh Elaheh, Prakhar Jaiswal, Rahul Rai, and Kemper Lewis. 2018. "From Conventional to Additive Manufacturing: Determining Component Fabrication Feasibility." In *International Design Engineering Technical Conferences and Computers and Information in Engineering Conference*, Vol. 51753, V02AT03A043. American Society of Mechanical Engineers.

Goodfellow, Ian J., Jean Pouget-Abadie, Mehdi Mirza, Bing Xu, David Warde-Farley, Sherjil Ozair, Aaron Courville, and Yoshua Bengio. 2014. "Generative Adversarial Networks".

Gordon, Jerard V., Sneha P. Narra, Ross W. Cunningham, He Liu, Hangman Chen, Robert M. Suter, Jack L. Beuth, and Anthony D. Rollett. 2020. "Defect Structure Process Maps for Laser Powder Bed Fusion Additive Manufacturing." *Additive Manufacturing* 36: Artlcle ID 101552. doi:10.1016/j.addma.2020.101552.

Gupta, Sulabh, and Rahul Rai. 2014. "A Graph Grammar Based Approach to 3D Print and Assemble Furniture." In *2014 International Solid Freeform Fabrication Symposium*, University of Texas at Austin.

Hochreiter, Sepp, and Jürgen Schmidhuber. 1997. "Long Short-Term Memory." *Neural Computation* 9 (8): 1735–1780. doi:10.1162/neco.1997.9.8.1735.

Jaiswal, Prakhar, and Rahul Rai. 2019. “A Geometric Reasoning Approach for Additive Manufacturing Print Quality Assessment and Automated Model Correction.” *Computer-Aided Design* 109: 1–11. doi:10.1016/j.cad.2018.12.001.

Kamath, Chandrika, Bassem El-Dasher, Gilbert F. Gallegos, Wayne E. King, and Aaron Sisto. 2014. “Density of Additively-manufactured, 316L SS Parts Using Laser Powder-bed Fusion At Powers Up to 400 W.” *The International Journal of Advanced Manufacturing Technology* 74 (1-4): 65–78. doi:10.1007/s00170-014-5954-9.

Kempen, K., L. Thijs, E. Yasa, M. Badrossamay, W. Verheecke, and J. P. Kruth. 2011. “Process Optimization and Microstructural Analysis for Selective Laser Melting of AlSi10Mg.” In *Solid Freeform Fabrication Symposium, Austin TX*, Vol. 22, 484–495.

Khadilkar, Aditya, Jun Wang, and Rahul Rai. 2019. “Deep Learning–Based Stress Prediction for Bottom-Up SLA 3D Printing Process.” *The International Journal of Advanced Manufacturing Technology* 102 (5): 2555–2569. doi:10.1007/s00170-019-03363-4.

Khairallah, Saad A., Andrew T. Anderson, Alexander Rubenchik, and Wayne E. King. 2016. “Laser Powder-Bed Fusion Additive Manufacturing: Physics of Complex Melt Flow and Formation Mechanisms of Pores, Spatter, and Denudation Zones.” *Acta Materialia* 108: 36–45. doi:10.1016/j.actamat.2016.02.014.

Khorram Niaki, Mojtaba, and Fabio Nonino. 2017. “Additive Manufacturing Management: A Review and Future Research Agenda.” *International Journal of Production Research* 55 (5): 1419–1439. doi:10.1080/00207543.2016.1229064.

Kruth, J.-P., G. Levy, F. Klocke, and T. H. C. Childs. 2007. “Consolidation Phenomena in Laser and Powder-Bed Based Layered Manufacturing.” *CIRP Annals* 56 (2): 730–759. doi:10.1016/j.cirp.2007.10.004.

Kunovjanek, Maximilian, and Gerald Reiner. 2020. “How Will the Diffusion of Additive Manufacturing Impact the Raw Material Supply Chain Process?.” *International Journal of Production Research* 58 (5): 1540–1554. doi:10.1080/00207543.2019.1661537.

Lane, Brandon, S. Mekhontsev, S. Grantham, Mihaela Vlasea, Justin Whiting, Ho Yeung, Jason Fox, et al. 2016. “Design, Developments, and Results from the NIST Additive Manufacturing Metrology Testbed (AMMT).” In *Solid Freeform Fabrication Symposium, Austin, TX*, 1145–1160.

Lane, Brandon, and Ho Yeung. 2020. “Process Monitoring Dataset From the Additive Manufacturing Metrology Testbed (AMMT): Overhang Part X4.” *Journal of Research of the National Institute of Standards and Technology* 125: 1–18. doi:10.6028/jres.125.027.

Liao, Kang, Chunyu Lin, Yao Zhao, and Moncef Gabbouj. 2019. “DR-GAN: Automatic Radial Distortion Rectification Using Conditional GAN in Real-Time.” *IEEE Transactions on Circuits and Systems for Video Technology* 30 (3): 725–733. doi:10.1109/TCSVT.76.

Liu, Ying, Rahul Rai, Anurag Purwar, Bin He, and Mahesh Mani. 2020. “Machine Learning Applications in Manufacturing.” *Journal of Computing and Information Science in Engineering* 20 (2): Artlcle ID 020301. doi:10.1115/1.4046427.

Lu, Yan, Zhuo Yang, Douglas Eddy, and Sundar Krishnamurty. 2018. “Self-Improving Additive Manufacturing Knowledge Management.” In *International Design Engineering Technical Conferences and Computers and Information in Engineering Conference*, Vol. 51739, V01BT02A016. American Society of Mechanical Engineers.

Mani, Mahesh, Brandon M. Lane, M. Alkan Donmez, Shaw C. Feng, and Shawn P. Moylan. 2017. “A Review on Measurement Science Needs for Real-Time Control of Additive Manufacturing Metal Powder Bed Fusion Processes.” *International Journal of Production Research* 55 (5): 1400–1418. doi:10.1080/00207543.2016.1223378.

Mertens, Raya, Sasan Dadbakhsh, J. Van Humbeeck, and J.-P. Kruth. 2018. “Application of Base Plate Preheating During Selective Laser Melting.” *Procedia CIRP* 74: 5–11. doi:10.1016/j.procir.2018.08.002.

Mirza, Mehdi, and Simon Osindero. 2014. “Conditional Generative Adversarial Nets.” *arXiv preprint arXiv:1411.1784*.

Mower, Todd M., and Michael J. Long. 2016. “Mechanical Behavior of Additive Manufactured, Powder-Bed Laser-Fused Materials.” *Materials Science and Engineering: A* 651: 198–213. doi:10.1016/j.msea.2015.10.068.

Ocylok, Sörn, Eugen Alexeev, Stefan Mann, Andreas Weisheit, Konrad Wissenbach, and Ingomar Kelbassa. 2014. “Correlations of Melt Pool Geometry and Process Parameters During Laser Metal Deposition by Coaxial Process Monitoring.” *Physics Procedia* 56: 228–238. doi:10.1016/j.phpro.2014.08.167.

Pal, Deepankar, Nachiket Patil, Kai Zeng, and Brent Stucker. 2014. “An Integrated Approach to Additive Manufacturing Simulations Using Physics Based, Coupled Multiscale Process Modeling.” *Journal of Manufacturing Science and Engineering* 136 (6). doi:10.1115/1.4028580.

Petridis, Stavros, Zuwei Li, and Maja Pantic. 2017. “End-to-End Visual Speech Recognition With LSTMs.” In *2017 IEEE International Conference on Acoustics, Speech and Signal Processing (ICASSP)*, 2592–2596. IEEE.

Rai, Rahul, and Prakhar Jaiswal. 2021. “Method for Automated 3D Print Quality Assessment and Redesign.” Oct. 21. US Patent App. 17/267,430.

Ramos-Grez, Jorge Andrés, and Mihir Sen. 2019. “Analytical, Quasi-stationary Wilson-Rosenthal Solution for Moving Heat Sources.” *International Journal of Thermal Sciences* 140: 455–465. doi:10.1016/j.ijthermalsci.2019.03.017.

Rubenchik, Alexander M., Wayne E. King, and Sheldon S. Wu. 2018. “Scaling Laws for the Additive Manufacturing.” *Journal of Materials Processing Technology* 257: 234–243. doi:10.1016/j.jmatprotec.2018.02.034.

Salomon, David. 2004. *Data Compression: The Complete Reference*. Springer Science & Business Media.

Scime, Luke, and Jack Beuth. 2018a. “Anomaly Detection and Classification in a Laser Powder Bed Additive Manufacturing Process Using a Trained Computer Vision Algorithm.” *Additive Manufacturing* 19: 114–126. doi:10.1016/j.addma.2017.11.009.

Scime, Luke, and Jack Beuth. 2018b. “A Multi-Scale Convolutional Neural Network for Autonomous Anomaly Detection and Classification in a Laser Powder Bed Fusion Additive Manufacturing Process.” *Additive Manufacturing* 24: 273–286. doi:10.1016/j.addma.2018.09.034.

Sharma, Ajit, Zhibo Zhang, and Rahul Rai. 2021. “The Interpretive Model of Manufacturing: A Theoretical Framework and Research Agenda for Machine Learning in Manufacturing." *International Journal of Production Research* 59 (16): 4960–4994. doi:10.1080/00207543.2021.1930234.

Shevchik, Sergey A., Christoph Kenel, Christian Leinenbach, and Kilian Wasmer. 2018. "Acoustic Emission for in Situ Quality Monitoring in Additive Manufacturing Using Spectral Convolutional Neural Networks." *Additive Manufacturing* 21: 598–604. doi:10.1016/j.addma.2017.11.012.

Singh, Shubhendu Kumar, Ruoyu Yang, Amir Behjat, Rahul Rai, Souma Chowdhury, and Ion Matei. 2019. "PI-LSTM: Physics-Infused Long Short-Term Memory Network." In *2019 18th IEEE International Conference on Machine Learning and Applications (ICMLA)*, 34–41. IEEE.

Spierings, Adriaan B., Thomas L. Starr, and Konrad Wegener. 2013. "Fatigue Performance of Additive Manufactured Metallic Parts." *Rapid Prototyping Journal*. 19 (2): 88–94. doi:10.1108/13552541311302932.

Stanisavljevic, Darko, David Cemernek, Heimo Gursch, Günter Urak, and Gernot Lechner. 2020. "Detection of Interferences in an Additive Manufacturing Process: An Experimental Study Integrating Methods of Feature Selection and Machine Learning." *International Journal of Production Research* 58 (9): 2862–2884. doi:10.1080/00207543.2019.1694719.

Thijs, Lore, Frederik Verhaeghe, Tom Craeghs, Jan Van Humbeeck, and Jean-Pierre Kruth. 2010. "A Study of the Microstructural Evolution During Selective Laser Melting of Ti–6Al–4V." *Acta Materialia* 58 (9): 3303–3312. doi:10.1016/j.actamat.2010.02.004.

Wang, Zhou, Eero P. Simoncelli, and Alan C. Bovik. 2003. "Multiscale Structural Similarity for Image Quality Assessment." In *The Thrity-Seventh Asilomar Conference on Signals, Systems & Computers, 2003*, Vol. 2, 1398–1402. IEEE.

Weisstein, Eric W. 2005. "Moore Neighborhood." *Wolfram MathWorld*. https://mathworld.wolfram.com/MooreNeighborhood.html.

Wolterink, Jelmer M., Tim Leiner, Max A. Viergever, and Ivana Išgum. 2017. "Generative Adversarial Networks for Noise Reduction in Low-Dose CT." *IEEE Transactions on Medical Imaging* 36 (12): 2536–2545. doi:10.1109/TMI.2017.2708987.

Yadroitsau, Ihar. 2008. "Direct Manufacturing of 3D Objects by Selective Laser Melting of Metal Powders." PhD diss., Saint-Etienne.

Yang, Ruo-Yu, and Rahul Rai. 2019. "Machine Auscultation: Enabling Machine Diagnostics Using Convolutional Neural Networks and Large-Scale Machine Audio Data." *Advances in Manufacturing* 7 (2): 174–187. doi:10.1007/s40436-019-00254-5.

Yang, Ruoyu, Shubhendu Kumar Singh, Mostafa Tavakkoli, Nikta Amiri, Yongchao Yang, M. Amin Karami, and Rahul Rai. 2020. "CNN-LSTM Deep Learning Architecture for Computer Vision-Based Modal Frequency Detection." *Mechanical Systems and Signal Processing* 144: Artlcle ID 106885. doi:10.1016/j.ymssp.2020.106885.

Yang, Zhuo, Yan Lu, Ho Yeung, and Sundar Krishnamurty. 2019. "Investigation of Deep Learning for Real-Time Melt Pool Classification in Additive Manufacturing." In *2019 IEEE 15th International Conference on Automation Science and Engineering (CASE)*, 640–647. IEEE.

Yang, Zhuo, Yan Lu, Ho Yeung, and Sundar Kirshnamurty. 2020. "3D Build Melt Pool Predictive Modeling for Powder Bed Fusion Additive Manufacturing." In *International Design Engineering Technical Conferences and Computers and Information in Engineering Conference*, Vol. 83983, V009T09A046. American Society of Mechanical Engineers.

Yang, Zhuo, Yan Lu, Ho Yeung, and Sundar Krishnamurty. 2020. "From Scan Strategy to Melt Pool Prediction: A Neighboring-Effect Modeling Method." *Journal of Computing and Information Science in Engineering* 20 (5). doi:10.1115/1.4046335.

Yeung, H., B. M. Lane, M. A. Donmez, J. C. Fox, and J. Neira. 2018. "Implementation of Advanced Laser Control Strategies for Powder Bed Fusion Systems." *Procedia Manufacturing* 26: 871–879. doi:10.1016/j.promfg.2018.07.112.46th SME North American Manufacturing Research Conference, NAMRC 46, Texas, USA.

Yeung, Ho, Zhuo Yang, and L. Yan. 2020. "A Meltpool Prediction Based Scan Strategy for Powder Bed Fusion Additive Manufacturing." *Additive Manufacturing* 35: Artlcle ID 101383. doi:10.1016/j.addma.2020.101383.

Yuan, Bodi, Brian Giera, Gabe Guss, Ibo Matthews, and Sara Mcmains. 2019. "Semi-Supervised Convolutional Neural Networks for In-Situ Video Monitoring of Selective Laser Melting." In *2019 IEEE Winter Conference on Applications of Computer Vision (WACV)*, 744–753. IEEE.

Zhang, Baicheng, Lucas Dembinski, and Christian Coddet. 2013. "The Study of the Laser Parameters and Environment Variables Effect on Mechanical Properties of High Compact Parts Elaborated by Selective Laser Melting 316L Powder." *Materials Science and Engineering: A* 584: 21–31. doi:10.1016/j.msea.2013.06.055.

Zhang, Bin, Shunyu Liu, and Yung C. Shin. 2019. "In-Process Monitoring of Porosity During Laser Additive Manufacturing Process." *Additive Manufacturing* 28: 497–505. doi:10.1016/j.addma.2019.05.030.

Zhang, Binbin, Prakhar Jaiswal, Rahul Rai, Paul Guerrier, and George Baggs. 2019. "Convolutional Neural Network-Based Inspection of Metal Additive Manufacturing Parts." *Rapid Prototyping Journal*. 25 (3): 530–540. doi:10.1108/RPJ-04-2018-0096.

Zhang, Binbin, Prakhar Jaiswal, Rahul Rai, and Saigopal Nelaturi. 2018. "Additive Manufacturing of Functionally Graded Material Objects: A Review." *Journal of Computing and Information Science in Engineering* 18 (4): 041002. doi:10.1115/1.4039683.

Zhang, Yaqi, Vadim Shapiro, and Paul Witherell. 2020. "A Neighborhood-Based Neural Network for Melt Pool Prediction and Control." In *International Design Engineering Technical Conferences and Computers and Information in Engineering Conference*, Vol. 83983, V009T09A026. American Society of Mechanical Engineers.

Zhang, Yi, and Jing Zhang. 2019. "Modeling of Solidification Microstructure Evolution in Laser Powder Bed Fusion Fabricated 316L Stainless Steel Using Combined Computational Fluid Dynamics and Cellular Automata." *Additive Manufacturing* 28: 750–765. doi:10.1016/j.addma.2019.06.024.

Zhang, Zhibo, Prakhar Jaiswal, and Rahul Rai. 2018. "Featurenet: Machining Feature Recognition Based on 3D Convolution Neural Network." *Computer-Aided Design* 101: 12–22. doi:10.1016/j.cad.2018.03.006.